

Article

Micro-Macro Relationship between Microstructure, Porosity, Mechanical Properties, and Build Mode Parameters of a Selective-Electron-Beam-Melted Ti-6Al-4V Alloy

Giovanni Maizza ^{1,*} , Antonio Caporale ¹ , Christian Polley ² and Hermann Seitz ^{2,3} ¹ Department of Applied Science and Technology, Politecnico di Torino, 10129 Torino, Italy² Microfluidics, Faculty of Mechanical Engineering and Marine Technology, University of Rostock, 18059 Rostock, Germany³ Department Life, Light & Matter, University of Rostock, 18059 Rostock, Germany

* Correspondence: maizza@polito.it; Tel.: +39-011-090-4632

Received: 12 June 2019; Accepted: 10 July 2019; Published: 15 July 2019



Abstract: The performance of two selective electron beam melting operation modes, namely the manual mode and the automatic ‘build theme mode’, have been investigated for the case of a Ti-6Al-4V alloy (45–105 μm average particle size of the powder) in terms of porosity, microstructure, and mechanical properties. The two operation modes produced notable differences in terms of build quality (porosity), microstructure, and properties over the sample thickness. The number and the average size of the pores were measured using a light microscope over the entire build height. A density measurement provided a quantitative index of the global porosity throughout the builds. The selective-electron-beam-melted microstructure was mainly composed of a columnar prior β -grain structure, delineated by α -phase boundaries, oriented along the build direction. A nearly equilibrium $\alpha + \beta$ mixture structure, formed from the original β -phase, arranged inside the prior β -grains as an α -colony or α -basket weave pattern, whereas the β -phase enveloped α -lamellae. The microstructure was finer with increasing distance from the build plate regardless of the selected build mode. Optical measurements of the α -plate width showed that it varied as the distance from the build plate varied. This microstructure parameter was correlated at the sample core with the mechanical properties measured by means of a macro-instrumented indentation test, thereby confirming Hall-Petch law behavior for strength at a local scale for the various process conditions. The tensile properties, while attesting to the mechanical performance of the builds over a macro scale, also validated the indentation property measurement at the core of the samples. Thus, a direct correlation between the process parameters, microstructure, porosity, and mechanical properties was established at the micro and macro scales. The macro-instrumented indentation test has emerged as a reliable, easy, quick, and yet non-destructive alternate means to the tensile test to measure tensile-like properties of selective-electron-beam-melted specimens. Furthermore, the macro-instrumented indentation test can be used effectively in additive manufacturing for a rapid setting up of the process, that is, by controlling the microscopic scale properties of the samples, or to quantitatively determine a product quality index of the final builds, by taking advantage of its intrinsic relationship with the tensile properties.

Keywords: EBM; SEBM; macro-instrumented indentation test; property-microstructure-process relationship; mechanical properties; indentation hardness; indentation modulus; tensile properties; Ti-6Al-4V alloy; α -platelet thickness; columnar microstructure

1. Introduction

The selective electron beam melting process (SEBM) is a tool-free additive manufacturing technology that enables the fabrication of complex, nearly net-shaped 3D products of dense, micro-architected structures, cellular structures, and open cell foam structures in which an electron beam is computer-controlled to selectively melt the powder feedstock and rise the build layer-by-layer. When SEBM is applied to a Ti-6Al-4V alloy, a wide range of outstanding properties (e.g., excellent biocompatibility, specific strength, stress corrosion cracking resistance, good ballistic resistance, and thermal stability) as well as intricate structures (e.g., cellular, open porosity, and gradient) can be obtained, which enable it to be used for biomedical, aerospace, military, chemical, and motorsport applications [1–6]. Such a unique combination is particularly advantageous for lightweight applications or whenever high specific mechanical properties and cost advantages are favorable compared to conventional machining [4,7].

SEBM has become a mature technology that can rely on an extensive amount of literature, which aids the development of new applications [6]. Powder flowability plays a crucial role in the initial raking of layers which, in turn, determines the optimal density and homogeneity of a microstructure after solidification [7].

Solidified SEBM microstructures are relatively fine [8,9] and frequently free of martensite, unless special SEBM conditions or very fine powders are selected, or very thin parts are fabricated [3,10,11].

The absence of martensite is one of the main causes of the observed reduced mechanical properties of SEBM products compared to their selective laser melting (SLM) counterparts [12–14], although additional factors, such as the initial powder (average size and size distribution), part thickness, and oxygen uptake, are also relevant.

Nevertheless, the mechanical performances of SEBM-manufactured Ti-6Al-4V and Ti-6Al-4V ELI alloy products [10,12,14–16] compare well with those fabricated by means of SLM [8,12–14] and those produced by means of conventional casting and wrought routes [14,17].

It has been shown that a large range of other outstanding properties [10,12,15,18,19] can currently be achieved in SEBM-manufactured builds as a result of a better understanding of the interrelationship between process parameters (e.g., scan speed, offset focus and beam current, beam current, layer feed, offset focus, and melting paths, etc.) and of such crucial factors as microstructure [10–12,14–16,20–24], chemical composition [14,25], particle size and distribution of pre-alloyed powders [26], the electrostatic charge effect in the powder [22], powder pre-heating [22,23], sintering conditions of the powder (prior to melting) [22,24], build thickness [11,14,15], surface quality (i.e., roughness and topography), [14,15], grindability (to minimize wear resistance and dissipation by friction) [12,21], bioreactivity [21], corrosion resistance [12], porosity [10,11,14–16,23,24,27], building orientation (horizontal and vertical) [10,14], distance from the build plate [15], and clean-up effect of the part upon shot-peening [24].

Among the available literature, the following studies share some common features with the present research.

Puebla et al. [10], for instance, investigated the effect of scan speed on the microstructure resolution and tensile properties of a Ti-6Al-4V alloy and found that horizontal and vertical (cylindrical rod) builds exhibited different microstructures, that is, they were coarser in the former case and much finer in the latter. An acicular α -phase and an $\alpha + \beta$ structure were found for a low scan speed (0.1 m/s), but a mixture of a highly resolved lamellar α -phase and α' -phase was observed for much higher scan speeds (1 m/s) and for a relatively small powder size (30 μm). However, in general, the presence of an α' -phase is rarely observed in the SEBM of coarse powder (45–100 μm), even at very high scan speeds, although it might be more likely, in both SEBM and SLM, for small Ti-6Al-4V alloy powders ($\sim 30 \mu\text{m}$) at very high scan speeds [10].

Murr et al. [3] related the scan speed of the beam to the residual properties and to the mechanical performances of the castings via the changes in the characteristic α -plate width, phase transformation, and dislocation density, and found that these were determined by the local temperature gradient and cooling rate. The observed columnar grain structures included acicular α -phase (hcp) and β -phase

(bcc) boundary transition phases [3]. A correlation between the α -platelet width and hardness revealed that the finer the local α -lamellae were, the higher the local hardness [10]. Although increasing the scan speed is a workable expedient that may be used to promote high-resolved microstructures (due to the inherently augmented solidification rate), it actually counteracts a detrimental increase in global porosity due to the increased volume of unmelted/unsintered powder [10].

However, two critical aspects of SEBM of the Ti-6Al-4V alloy which are somehow linked to each other have been identified, with these being firstly the designed fixed temperature control strategy used to control the SEBM process and secondly the resulting ambiguous relationship between the intrinsic microstructure gradient (along the build direction) [25,28] and the measured tensile properties.

It should be recalled that the temperature in the chamber is controlled by a thermocouple located below the build plate (stainless steel). As the build grows along the z-direction, the measured temperature becomes less and less representative of the actual energy injected by the beam into the layer. Moreover, this poor temperature control of the process is responsible for weak correlation between the SEBM parameters and the microstructural and mechanical properties of any alloy but of the Ti-6Al-4V alloy in particular [29,30].

According to current investigations, the tensile properties of an SEBM product provide a rough indication of the mechanical response of their build-scale microstructure, which may include phase gradients of different composition, distribution, and resolution, etc. As a result, the reported relationships between the microstructure and the tensile properties cannot be considered univocal. The search for a local scale relationship rather than a build-scale one would be more profitable for optimization purposes provided that the microstructure is mechanically tested at a local scale. To the best of the authors' knowledge, no studies have so far dealt with macro-instrumented indentation tests on SEBM-fabricated parts, which is one of the few available standard methods allowing the local measurement of tensile-like properties. However, to this end the works of SridharBabu et al. [31], Puebla et al. [10], and Lancaster et al. [32] are worth mentioning. The former authors tested a Ti-6Al-4V alloy by means of a nano-instrumented indentation test at various strain rates, mainly to elucidate the indentation size effect (instead of measuring the local tensile-like properties). The next authors [10] complemented the tensile tests with conventional macro-hardness (Rockwell-C, 1.5 kN load) and micro-hardness (Vickers, 0.1 N load) tests in their attempt to establish a relationship between porosity evolution and microstructure changes as a function of scan speed. Interestingly, they found that the micro-Vickers test provided hardness information on the local microstructure and the Rockwell hardness test accounted for macroscale porosity due to the larger imposed load.

Lancaster et al. [32] performed small punch tests on miniaturized thin disk-shaped specimens from various discrete locations in a Ti-6Al-4V thin-walled complex geometry component. They were able to analyze both the fracture behavior of various fabricated layers and the influence of the local porosity. However, the measured test curves were of a force-displacement type rather than of a stress-strain type. Moreover, the used thin samples required very accurate and time-consuming preparation.

On the other hand, the standard macro-instrumented indentation test [33] offers a quick, low cost, and non-destructive alternative to effectively sense tensile-like properties in either build components or ad hoc reference samples. Such a testing method has been used in this study to interrelate the local mechanical properties to the local microstructure and ultimately to optimize the process parameters.

However, there exists an urgent need to control the microstructure of SEBM products for a specified application, especially in the case of intricate geometries. This goal is currently achieved by selecting a single (blind) standard build theme mode (BTM) which can be used for any geometry. Although such a mode has been designed to be self-adaptive, it often appears to be unsatisfactory. Thus, it seems more efficient and effective to use customized process windows for each application. Hrabe et al. [15] took a step forward in this direction. They explored how user-setting parameters, denoted as the manual building mode (MM), compared with the BTM mode (default mode recommended by Arcam EBM®) in terms of microstructure and mechanical properties measured at different distances from the build plate for different thicknesses of the build.

The present study, which was inspired by the work of Hrabe et al. [15], was undertaken with the primary aim of strengthening the understanding of the complex relationship that exists, at various local regions of Ti-6Al-4V alloy build samples, between the porosity, microstructure, and mechanical properties for two build modes, namely BTM (Arcam EBM[®] A1 device) and MM. A unique strategy of the research developed here is the application of the macro-instrumented indentation test (MIIT), due to its efficient, easy, and quick testing features as well as its suitability to benchmark SEBM products through the non-destructive determination of local tensile-like properties.

2. Materials and Methods

A schematic setup of the employed Arcam EBM[®] A1 (Arcam AB, Mölndal, Sweden) device is shown in Figure 1.

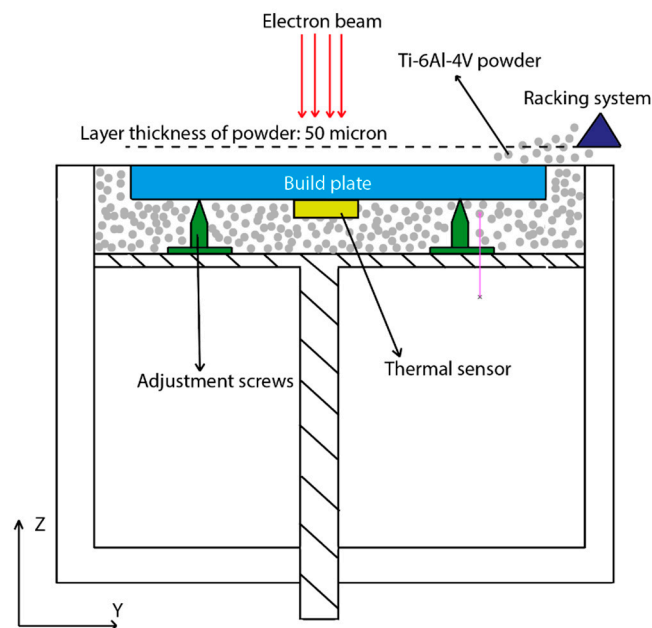


Figure 1. Schematic of the employed Arcam EBM[®] A1 device.

The z-axis is the build direction and the x-z plane is the build plane. The build plate ($210 \times 210 \times 10 \text{ mm}^3$) is made of stainless steel. It is stabilized by four supports which protect against accidental vibrations or shocks. The vacuum, acceleration voltage, and maximum temperature range are accurately controlled ($2 \times 10^{-2} \text{ mBar}$, 60 kV, and 600–650 °C, respectively). Any water vapor and/or oxygen gas is extracted from both the chamber and the build plate during the evacuation stage, which lasts approximately ten minutes. A high vacuum is needed to enable the functioning of the electron beam gun and to prevent oxidation of the powders, especially the titanium alloy powder [4]. A thermocouple placed on the bottom face of the build plate permits the process temperature to be monitored over time. It should be noted that the aforementioned temperature is just an indicative temperature that is affected by the material properties and thickness of the build plate and by the built geometry. As the basic principles of operation and hardware setup of SEBM are well-known (see for example [3,28,34]) only the information pertinent to this study are detailed hereafter. The SEBM process runs using the following four basic steps: firstly, spreading the powder bed to a preset thickness; secondly, pre-heating the powder bed at a low beam power; thirdly, melting the powder layer at a controlled scan rate and beam current; and fourthly, cooling to room temperature in the chamber. In this study, the chamber volume was filled with pre-alloyed Ti-6Al-4V powder (Arcam[®] Ti64) with a 45–105 μm nominal particle size distribution. Figure 2 shows that the powder is mostly composed of regular spherical particles. However, a number of intrinsic defects, such as entrapped gas, surface impurities, and collapse of particles, which are typical of atomized particles, are also apparent.

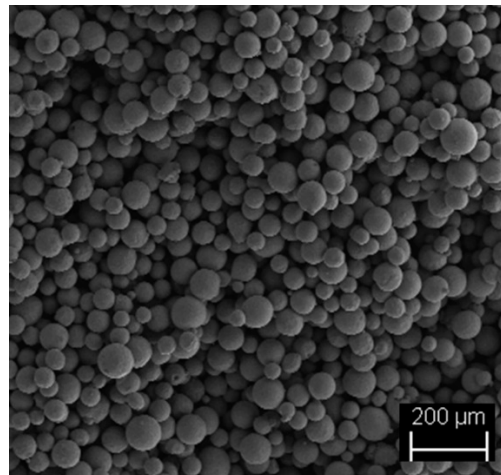


Figure 2. SEM image of the Ti-6Al-4V pre-alloyed powder used in the experiments.

In the first step, the powder was uniformly raked onto the surface of the build plate to a layer thickness of $\sim 100\ \mu\text{m}$. In the second step, preheating started as soon as a $\sim 5 \times 10^{-4}$ mBar vacuum was attained in the chamber. Both the build plate and the Ti-6Al-4V alloy powder were pre-heated to $\sim 730\ ^\circ\text{C}$ using a low (defocused) current beam and a high scan rate. The partial sintering of the particles determined a sudden beneficial increase in thermal conductivity across the deposited layer. By increasing the beam current, a temperature regime of $730\ ^\circ\text{C}$ was attained at the build plate during the actual melting step whereas vacuum in the chamber was maintained at 2×10^{-3} mBar in the temperature range of $600\text{--}650\ ^\circ\text{C}$. At such a high beam power, a continuous flow of high-purity helium prevents the particles from being charged and augments the cooling of the build. The powder is held in place as the reduced charging of the particles avoids the powder blown phenomena [9,23]. Once the first layer had been deposited, the build plate was displaced downward by a distance that was equivalent to one layer thickness ($50\ \mu\text{m}$). Additional powder was fed from the dispenser and raked over the surface of the underlying solidified layer. The build grew layer by layer until it was complete.

In the last stage, the contour of the build was completely melted (contouring). Finally, the build surfaces were cleaned of any adhering pre-sintered or free powder particles by a vigorous powder jet blasting.

The in-line powder recovery system (PRS) is designed to withdraw the blasted and unprocessed powder from the previous melting step and to convey it to the dispenser, prior to accurate sieving, for use in the next cycle. It is expected that the oxygen content in the powder will increase slightly as the number of recycles increase [24,35].

SEBM is generally conducted using the default BTM by enabling the built-in 'speed function 98'. This sets the beam current and speed factor into an automatic control mode which is based on internal algorithms developed and optimized by Arcam[®] for a specified powder. The beam current is allowed to vary between two limits that may be set by the user. The speed factor is related to the beam current and scan speed. All the factors are controlled during SEBM as a black box by the BTM built-in function. The default BTM conditions have been optimized to achieve optimal builds in terms of soundness, microstructure, and properties.

In addition to BTM, the original research has investigated a large number of processing parameters and range limits in MM. However, only the most salient SEBM conditions are presented in this work. For each process parameter combination, a set of three samples was designed for a tensile test and one sample was designed for a microstructure inspection and macro-instrumented indentation test (MIIT). These samples were all taken from the center of the chamber as the center is affected less by electron beam instability. The microstructure and MIITs were analyzed at three locations (bottom A, core B, and top C) which were assumed as representative regions near to, at a mid-distance from (at the core), and far from the build plate surface [19].

The performances of MM and BTM on manufactured builds are generally discriminated in terms of porosity, microstructure, and mechanical properties. The BTM sample (baseline) is denoted hereinafter as the a-sample. The values of the process parameters in MM were selected in relation to the BTM ones. The beam current range was set to 15–20 mA and the scan speed was set to a fixed value of 4.53 m/s for BTM. Accordingly, the process parameters in MM were set as 15 mA and 4.53 m/s (denoted hereinafter as the b-sample), 15 mA and 5.9 m/s (denoted hereinafter as the c-sample), and 12 mA and 4.53 m/s (denoted hereinafter as the d-sample). The aforesaid value of 4.53 m/s was suggested by the BTM algorithm, whereas the choice of both the current range and speed limit was made on the basis of previous investigations [24,35].

The results collected from the BTM- and MM-processed samples are were then analyzed in terms of porosity, microstructure, and mechanical properties (tensile and MIIT). Three dog-bone shaped samples ($t = 6.10$ mm, $L = 102.10$ mm, $w = 12.40$ mm) for the three investigated MM conditions were horizontally built by SEBM (Figure 3a).

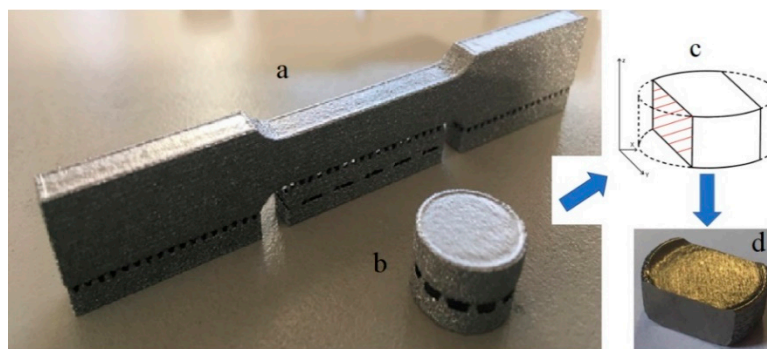


Figure 3. Build samples after shot peening: (a) as-build dog-shaped sample with supports, (b) as-build disk sample with supports; (c) schematic of cutting of disk sample to ensure two parallel and flat surfaces; (d) actual polished disk sample used for metallographic and macro-instrumented indentation test. Note that the flat cases are parallel to the build direction.

The samples were machined and then ground according to the ASTM E 466-96 standard. The tensile test procedure conformed with the ASTM E8/E8M-09 (other than the use of room temperature and a 1 mm/min strain rate) requirements. The disk samples (for optical and MIIT measurements) were fabricated with their axis perpendicular to the build plane (Figure 3b). After appropriate machining ($\text{Ø}15 \times 5.20$ mm), the disk samples were chordally cut from two opposite sides to a depth of 3 mm (Figure 3c,d) to ensure two perfectly parallel faces and then ground and polished to a mirror finish (1 μm diamond paste). For metallographic inspections, the samples were chemically etched using Kroll's reagent (0.1 L water, 5 mL nitric acid, and 2.5 mL hydrofluoric acid for about 3 s) [10].

As both faces were parallel to the build (z-axis) direction, these could therefore be used to assess both the local porosity and microstructure by means of an optical microscope (LEICA DMI 3000M) (Leica Microsystems GmbH, Wetzlar, Germany), and the local tensile-like properties were measured by an MIIT device prototype. The overall residual porosity (or density) in the sample disks was measured by means of Archimedes' principle.

3. Results and Discussion

3.1. Visual Inspection

First, the dog-shaped b–d samples and the disk-shaped a–d samples were inspected visually. Recall that the main features of the regular dog-bone shaped a-sample after being manufactured using BTM conditions have already been discussed [24]. The main features of the a-sample disk after processing may be summarized as follows: significant thermally-induced distortions in both the top (last deposited layer) and bottom (near the build plate) regions, despite the supports which were

bonded perfectly to the build plate. Such thermal distortions may be ascribed to excessive overheating (e.g., as a result of an improper choice of the limits in the variability range of the beam current and scan speed) and/or to uneven shrinkage on cooling. However, no similar distortions have been observed previously [24] under BTM, although the supports in this work had a different design. Thus, a different microstructure and mechanical properties could be expected in the currently considered a-sample, compared to the previously BTM built a-sample. The tensile b-sample shows even more pronounced thermal distortions (that is, those which were much larger at one end than at the other). The distortions were so significant that the supports were nearly completely detached from the build plate. The choice of fixed process parameters in MM processing very likely resulted in the beam current being much higher than that actually needed for a decreased scan speed. Instead, both the tensile and disk-shaped c-samples were less compromised than the a- and b-samples. Slight deformations were only visible on the top edge of the disk c-sample (last deposited layer) whereas the tensile samples complied with the specified design (sizes and tolerances) requirements. Both the tensile and disk d-sample were free of distortions, the edges were quite sharp, and design specifications were met aesthetically as well as dimensionally.

3.2. Porosity and Density

Pore counting was carried out optically over one of the two polished surfaces. An optical microscope was used in the differential interface contrast (DIC) mode at a 25 \times magnification level to permit analysis of the overall sample cross section in one single optical view field, that is, from the build plate to the last deposited layer. Only spherical or nearly spherical pores were counted. These pores were attributed to gases, such as argon, which were entrapped in the original atomized powder [16]. The entire sample thickness was divided into three regions along the build direction, i.e., A, B and C, which represent the bottom (near the build plate), center, and top (last deposited layer) regions, respectively. Figure 4 shows the most relevant pores detected over the entire build thickness in the a–d sample disks. The circles denote the largest observed pores under the selected view field. Other defects, such as unmelted or unsintered powder regions [10,16], are also visible, but have been ignored in the counting analysis because of their different origin.

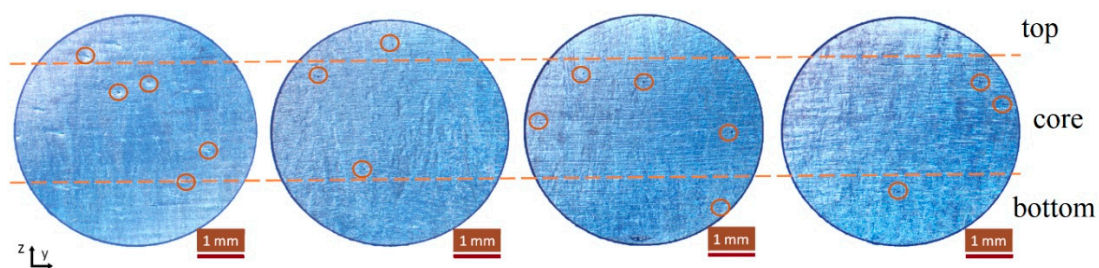


Figure 4. Porosity inspection in a–d samples under optical microscope (25 \times): circles denote largest observed pores.

The pores can be seen to be distributed over the whole building height, although there is a certain prominent population near the build plate. Their size varies from 100 to more than 500 μm . However, no such defects can be detected in either the b- or the d-sample disks.

To achieve more representative statistics by optical microscope, pore counting was repeated at a 200 \times magnification level. In such a manner, not only large but also relatively small pores were counted to determine porosity. The results in Figure 5 indicates that the number of pores and pore size ranges of the a–d samples were 17 and 15–37 μm , 20 and 11–29 μm , 6 and 12–45 μm , and 5 and 18–34 μm , respectively.

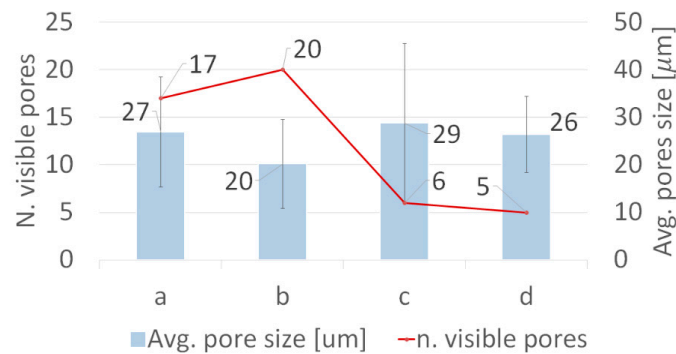


Figure 5. Total pore counting analysis of a–d samples by optical microscopy at 200 \times magnification: number of visible pores and average pore size.

It should be noted that in the a- and c-samples numerous new unmelted zones were detected at the higher optical resolution which were not apparent at the lower resolution. In summary, the b-sample exhibited the largest porosity but the smallest pore size, whereas the c-sample showed the smallest porosity but the largest pore size together with unmelted layer/particle defects. Furthermore, the average pore size of both the a- and d-samples was of the same order of magnitude, but the porosity of the a-sample was larger than that of the d-sample. Finally, we determined, on the basis of the porosity counting analysis, that the d-sample (MM: 12 mA and 4.53 m/s) was less affected than the a-sample (BTM: 15~20 mA and 4.53 m/s).

Further, a more reliable measure of the bulk porosity was able to be achieved via a density measurement using Archimedes' principle. The results show that the density remained approximately constant in all the samples ($\sim 4.39 \text{ g}\cdot\text{cm}^{-3}$), that is, $\sim 1\%$ lower than the theoretical density ($4.43 \text{ g}\cdot\text{cm}^{-3}$) of the alloy. It has emerged that the measured porosity was not the primary cause of the weight reduction of the samples. If necessary, porosity can be eliminated by a subsequent hot isostatic pressing (HIP) [14,21,36].

3.3. Microstructures

The microstructures of the a–d sample disks were inspected optically over the build height at the three regions A, B, and C. The identification of such three regions was necessary as one of the unique features of SEBM products is the formation of a typical gradient microstructure along the build direction, which, in turn, has a relevant impact on the mechanical performances of the product. It was observed, from the optical images, that all the samples had a predominant columnar structure as a consequence of the preferential heat dissipation along the build direction, except for the first layers. Figure 6 shows a general optical view of the microstructure of the a–d samples at the three specified regions over the build thickness. These images revealed that each building mode could be discriminated according to their respective microstructure morphology, porosity size, and porosity size distribution. The following sections present qualitative and quantitative details of the observed microstructures at the three representative regions after cooling for both the BTM and MM conditions (e.g., the a- to d-sample disks).

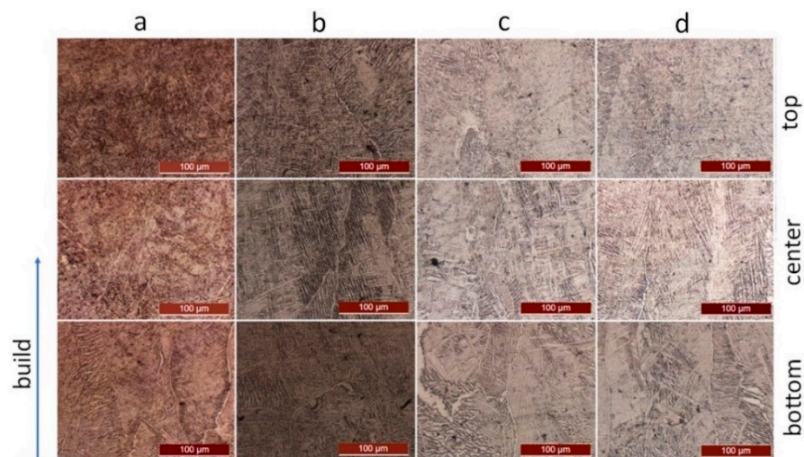


Figure 6. Collective set of optical images of microstructures (Kroll etchings) in the a–d samples as a function of the build distance from the build plate to the last deposited layer (bottom, center, and top) at 100 \times .

3.3.1. Bottom Region

Figure 7a–d shows the optical microstructures at the bottom region of the a–d sample disks. The nearest regions to the hot (isothermal) build plate (630 °C) first experienced a fast heating/melting at a high temperature and then underwent solidification under relatively low rate conditions down to the hot plate temperature. The observed equiaxed microstructure, which consists of prior β -grains delineated by a wavy and relatively thick α -phase boundary (bright), is indicative of a mild isotropic cooling from the melting temperature to the hot plate temperature (hereinafter denoted as first step cooling). Under such conditions, heat is spread from the layers almost uniformly in all directions.

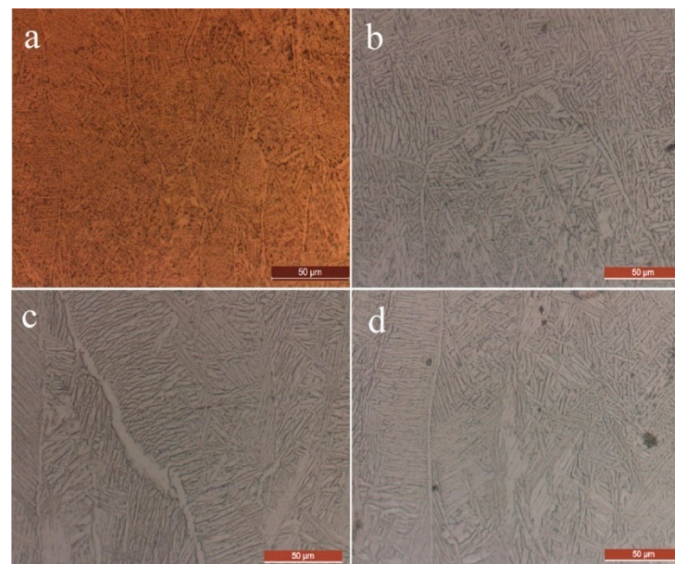


Figure 7. Optical images of microstructures in the bottom region (near the build plate) for the a–d sample disks.

The prior β -grains embedded a coarse $\alpha + \beta$ structure composed of β rods (dark) surrounding the α -lamellae, which were either in the form of a colony or basket weave pattern. This microstructure morphology and composition near the build plate is in accord with that found by Mandil et al. in a similar build location [19]. As the number of the overlying solidified layers (or distance from the build plate) increases, the microstructure tends to a more typical columnar prior β -grain structure delineated by a thinner α -phase boundary and a transformed $\alpha + \beta$ structure which are finer than their respective

counterparts in the A-region. Elongation of the prior β -grains increases as the separation distance from the build plate increases. Notice that the transition of the β -phase into the equilibrium $\alpha + \beta$ mixture (over the β -transus temperature range) takes place during the shutdown of the chamber, from the melting regime temperature (730 °C) to the room temperature (hereinafter denoted the secondary stage of cooling). In this stage the cooling rate is much lower than in the first step. Morphologies of such nearly equilibrium phases may vary considerably depending on the nature of the alloying elements dissolved in the β -phase. The average size of the prior β -grains in all the samples was greater than the thickness of the deposited layers. The primary β -grains in Figure 7 appear slightly elongated and surrounded by closed α -phase boundaries. The microstructure of the more remote overlying layers (i.e., those farthest from the build plate) appears to be finer than that in the A-region [25].

More sound properties of builds affected by BTM (a-sample) and MM (b–d samples) conditions may be extracted at a local scale rather than at a macroscopic (build) scale. The mechanical properties, whenever measured in a sufficiently small but representative volume of the build, can be directly related to more consistent microstructural features. The α -plate width can be utilized to discriminate the degree of local microstructure refinement induced by both processing modes. Although a more rigorous treatment should also include the α -colony width and the prior β -grain size, the latter are actually more difficult to discern under the SEBM conditions investigated here.

The BTM conditions in the a-sample originated smaller prior β -grains and the contours of the α -phase boundaries were bound more and were thinner (2–4 μm) than those of the MM specimens (4–10 μm). The nearly equilibrium microstructure consisted of α -lamellae arranged as either a colony or basket weave pattern together with a minor presence of the β -phase surrounding the α -lamellae [13,25]. However, the basket weave structure of the α -lamellae can be seen to be predominant in the d-sample (Figure 7d). It resembles the dendritic trees structures in conventional castings, in which the main branch (i.e., the α -phase boundary) first operates as the preferential nucleation site for new orthogonal side branches (i.e., the secondary α -phase colonies) whose boundaries, in turn, become preferential nucleation sites for new orthogonal side branches. The size of the prior β -grains in all the investigated samples was greater than the thickness of the deposited layers. Figure 8 shows the optically measured α -plate width values (averaged over ten measurements) for the a–d samples at the three characteristic regions over the sample thickness. The b-sample exhibited the largest α -plate width value ($3.13 \pm 0.8 \mu\text{m}$) compared with the lowest value ($1.93 \pm 0.44 \mu\text{m}$) in the a-sample. The c- and d-samples gave $2.28 \pm 0.33 \mu\text{m}$ (the smallest standard deviation) and $2.71 \pm 1.15 \mu\text{m}$ (the largest standard deviation), respectively. Thus, in general, BTM promoted finer microstructures than MM, which means that the built-in algorithm is more effective than keeping the selected process parameters constant.

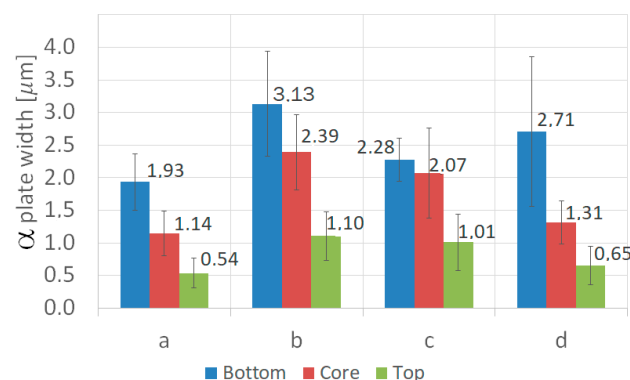


Figure 8. Average width of α -plates in the three regions across the thickness of the a–d sample disks.

3.3.2. Core Region

As the distance from the build plate increases, the prior β -grains become finer and more elongated along the build direction. The α -phase boundary is bound less (more open) than in the bottom region (see Figure 9).

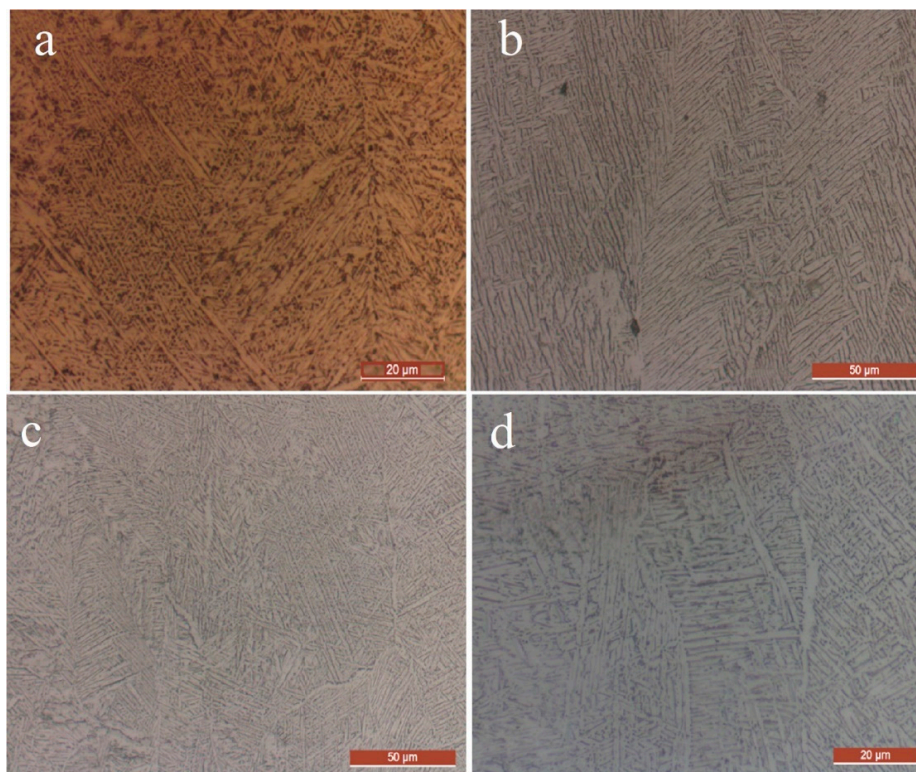


Figure 9. Optical images of microstructures in the core region for the a–d sample disks.

Such a new morphology echoes the stronger non-equilibrium conditions which induce larger solidification rates as a consequence of the larger temperature gradients (heat dissipation) and more anisotropic cooling along the build direction. As solidification is faster in the core region, atomic diffusion is proportionally hindered across the layers. The transformed microstructure at the core was found to be a mixture of the prevailing α -lamellar structure (with α -lamellae as a colony and basket weave pattern) over the minor surrounding β -phase. The average width of the α -plates at the core (B) of all samples was 20–30% lower than that at the bottom (A). In other words, the mean α -plate width in the a-sample was $1.14 \pm 0.34 \mu\text{m}$ (the smallest), whereas it was $2.39 \pm 0.58 \mu\text{m}$ (the largest), $2.07 \pm 0.69 \mu\text{m}$, and $1.31 \pm 0.33 \mu\text{m}$ for the b- to d-samples, respectively. The finer microstructures at the core region were again more effectively favored by BTM than MM.

3.3.3. Top Region

This region corresponds to the last deposited layers (C). As shown in Figure 10, the microstructure here is much finer than that found at the bottom (A). The interface between two adjacent prior β -grains is hardly discernable as a result of the stronger non-equilibrium conditions set in this region. The thickness of the α -phase boundary is not well defined.

The α -lamellae can be seen to be more elongated and thinner than those observed at the bottom (A). The relatively fine microstructure at the top is a consequence of the lower accumulation of heat, imparting lower annealing time, and faster dissipation of heat. However, no martensite structure may be detected, a result that is in contrast with other studies [11,25]. We believe that even within the limit of favorable cooling rate conditions for the formation of a metastable martensite during the first step of cooling, the subsequent cooling to room temperature inevitably causes a gradual decomposition of martensite into an equilibrium $\alpha + \beta$ structure as described by Tan et al. [11]. On the basis of the α -plate width measurement it appears that the microstructure at the top region (C) is nearly 70% finer than that at the bottom (A). The average α -plate widths for the a–d samples were found to be equal to $0.54 \pm 0.23 \mu\text{m}$, $1.10 \pm 0.37 \mu\text{m}$, $1.10 \pm 0.43 \mu\text{m}$, and $0.65 \pm 0.30 \mu\text{m}$, respectively.

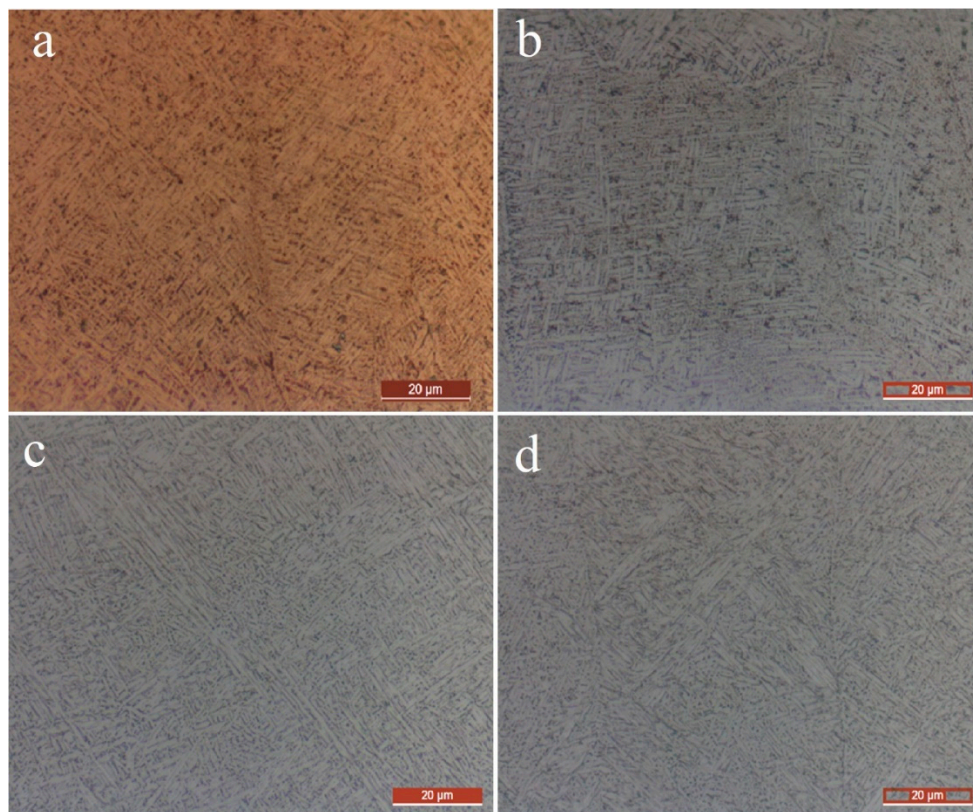


Figure 10. Optical images of microstructures in the top region (last deposited layer) for the a–d sample disks.

3.4. Tensile Test

It should be recalled that the behavior of the a-sample under tensile testing has already been presented in detail in a previous work [35]. All the remaining samples were tested in the present work. The cross-sectional area measured 36 mm^2 . The fracture in all the samples occurred within the gauge length (see Figure 11). The fracture behavior was found to be generally ductile in all the samples, in agreement with other works (for instance [23]), as it was promoted by the coalescence of microvoids [13]. The relevant mechanical properties (averaged over three specimens for each process condition) are compared in Figure 12 for clarity reasons. The measured properties were rather repeatable irrespective of the type of process condition.

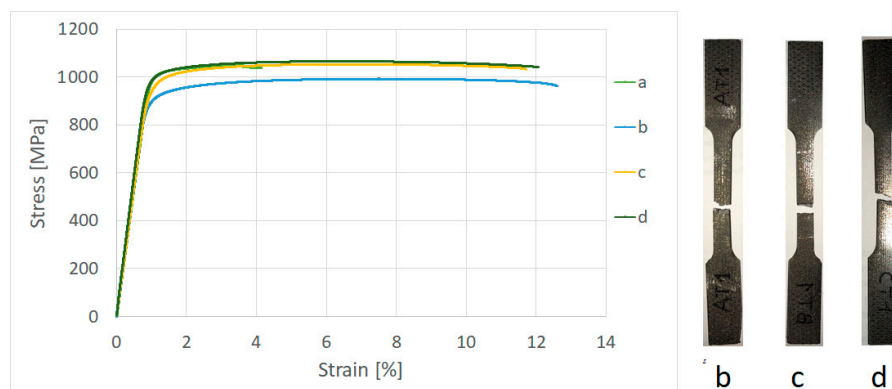


Figure 11. Engineering stress-strain curves of the a–d samples. Data for the a-sample is reported elsewhere [35].

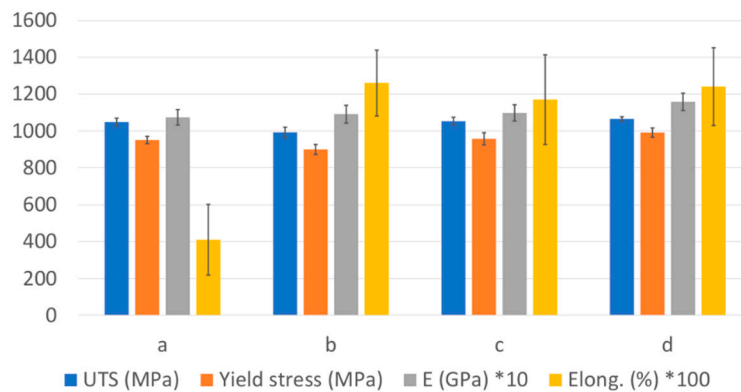


Figure 12. Tensile properties of a–d samples.

In all the cases, the measured UTS, being in the 1045–1065 MPa range, was larger than the 775 MPa [4], 928 MPa [13], 915 MPa [37], 959–990 MPa [2], 1010 MPa [23], and 930–1015 MPa values previously found for wrought Ti-6Al-4V alloys [38], except for that of the b-sample (~991 MPa). However, the latter compares well with other reported values [2,14]. On the other hand, Puebla et al. [10] have reported slightly larger values (980–1080 MPa), and Murr et al. [3] and Gaytan et al. [16] much larger ones, that is, 1150–1200 MPa and 1100–1400 MPa, respectively, than the present values. The UTS and YS values measured here were found to be both larger than those found in cold worked and annealed samples [37]. The measured elongations to fracture (10–12.4%) were larger than those found in SLM samples [3,13] and other SEBM samples [4,10,13], although other authors [2,3,18,23] have claimed much larger tensile ductility than that reported here.

A direct comparison of BTM and MM shows that both modes determined nearly identical UTS values (1047 versus 992–1065 MPa, respectively). The larger UTS values encountered in the a-, c-, and d-samples may be ascribed to their finer microstructure (α -plate width). Conversely, the low UTS value of the b-sample may mainly be attributed to its coarser microstructure (with only a minor contribution of porosity). Similar considerations apply to yield stress. Taking into account porosity itself, it is possible to rationalize that such defects are not of primary concern for mechanical properties in either BTM or MM, provided that they are not excessive, as was the case here for the b-sample. The UTS of the latter was in fact 992 MPa (the lowest) versus 1065, 1052, and 1047 MPa for the a-, c-, and d-samples, respectively. The Young modulus was 107 GPa (the smallest) in the a-sample, 116 GPa (the largest) in the d-sample and intermediate in the c- and b-samples. The elongation to fracture was nearly equal in all the samples and was in the 11.7–12.6% range.

3.5. Macro-Instrumented Indentation Test

The basic features of the used MIIT [39] and its advantages when applied to additive manufactured parts have already been discussed [40]. When dealing with additive manufactured parts, MIIT is more appropriate than the commonly used nano-instrumented indentation test, as the sensed volume in the former is representative of the typical microstructure of the builds and of the same order of magnitude as that involved in a tensile test. In the observed SEBM microstructures, the β -grain is the larger microstructure feature which embeds other smaller features. The average size of β -grains may exceed 50 μm in width and more than 100 μm in length. Thus, an adequate representative volume of the microstructure to be sensed mechanically should have an average edge larger than 100 μm . In this condition, the relevant indentation properties extracted from the MIIT, according to the ISO 14577-1 standard [33], can be directly linked with the tensile properties. As MIIT allows for a local measurement of mechanical properties it can virtually be performed at any point of the build in a quick and non-destructive manner. In this work the optimal peak load of 300 N was determined by trial and error, depending on the largest and smallest microstructure features to be sensed (see Figure 7, Figure 9, Figure 10, and Figure 13). This load assures test repeatability and absence of undesirable size effects,

and, more importantly, the indentation volume (underneath the Vickers indenter) was “representative” (i.e., contained the essential features) of the characteristic SEBM microstructures for each process condition. The sample disks previously used for porosity and microstructure analysis were then MIITed to assess the mechanical properties at the local scale. The indentation cycle included 60 s for loading, 60 s for holding, and 40 s for unloading. Each MIIT consisted of four repeated indentations at the same indent (Figure 13), although the indentation properties were extracted from the first cycle of the indentation curves. The choice of the B region for indentation is suggested here because it was affected by intermediate SEBM conditions between the two extreme ones, these being the isothermal condition near the build plate and the strong non-equilibrium condition at the build surface.

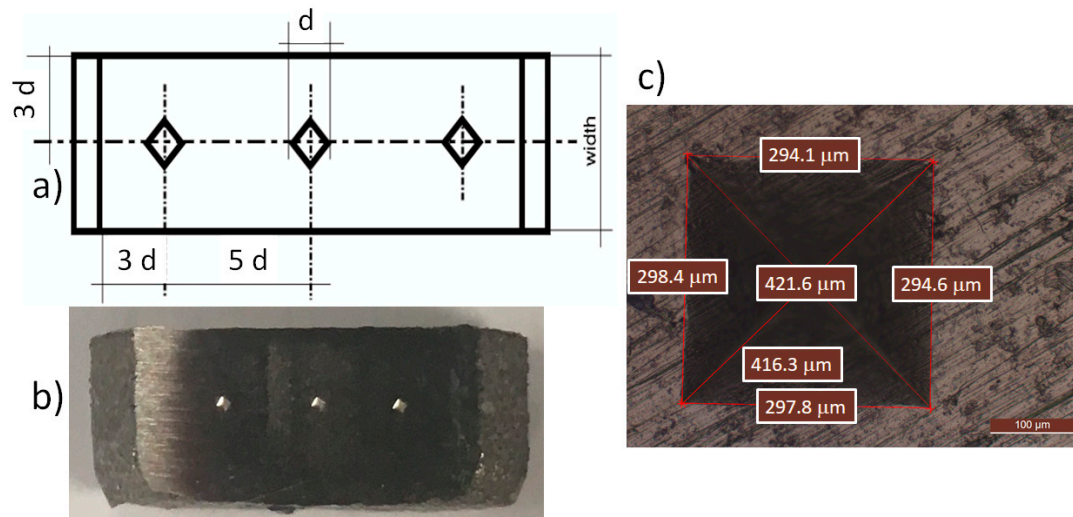


Figure 13. Macro-instrumented indentation test (MIIT) at the center: (a) separation distance between indents; (b) actual Vickers indentations; (c) typical Vickers macro-imprint in the b-sample.

The extracted indentation properties [33] were averaged over three indentations at three different locations in the B region. The typical MIIT curves for the given Ti-6Al-4V alloy are shown in Figure 14. The measured maximum penetration depth (h_{max}) was nearly equal for the b-, c-, and d-samples (in the 66.5–66 μm range), whereas that for the a-sample was 61 μm (lowest). The plastic penetration depth (h_p) was in the 53–52 μm range for the c- and b-samples and was ~ 50 μm for both the a- and d-samples (lowest).

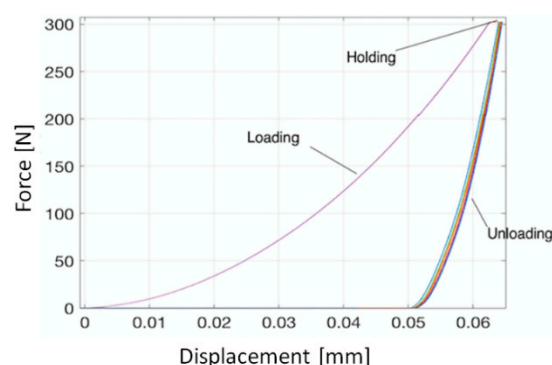


Figure 14. Typical macro-instrumented indentation load-displacement curves (four cycles in the same indent) at a 300 N peak load for the Ti-6Al-4V alloy.

A useful index of mechanical performance in industry is hardness. MIIT provides the so-called indentation hardness (H_{IT}). H_{IT} can be related to the equivalent Vickers hardness ($HV_{eq} = 0.0945 H_{IT}$), which allows direct comparisons with literature values based on conventional Vickers hardness. In this

work, the results show that H_{IT} progressively decreases from the a-sample (3.84 GPa) to the d-sample (3.56 GPa) to the c-sample (3.46 GPa) to the b-sample (3.36 GPa). When these values are converted into HV_{eq} (363, 336, 327, and 318, respectively) results that they are in fairly good agreement with other works [2,13,19,37] for an SEBM-manufactured Ti-6Al-4V alloy.

Obviously, it should be born in mind that hardness is a local property which varies according to the build thickness and the distance from the build plate [8]. Furthermore, it is well-known that hardness decreases as the size of the characteristic microstructure features increase [10]. Thus, it could be useful to attempt establish a local (B region) correlation between HV_{eq} and the α -plate width (λ). It has been confirmed that HV_{eq} is greater for finer microstructures and lower for coarser ones; more precisely, in this work, $362/\lambda = 0.8\text{--}1.5 \mu\text{m}$, $318/\lambda = 1.8\text{--}3 \mu\text{m}$, $326/\lambda = 1.3\text{--}2.7 \mu\text{m}$, and $336/\lambda = 0.97\text{--}1.66 \mu\text{m}$ for the a-sample through to the d-sample, respectively, which points out an approximate linear relationship between HV_{eq} and λ . Hrabe et al. [15] reported a Vickers hardness range of 345–360 for an SEBM-casted Ti-6Al-4V alloy, which is in good agreement with the hardness measured at the sample core of the a- and d-samples with quite fine microstructures.

However, finer microstructures may be favored by promoting more intensive heating, although this also causes undesirable distortions, especially in relatively thin parts, such as in flat tensile samples. This tendency has also been confirmed for the indentation properties. In fact, the greater the residual penetration depth (h_p) is, the lower the indentation hardness (H_{IT}) and the lower the indentation modulus (E_{IT}) in the b- and c-samples, compared to the other samples.

In an instrumented indentation test, the repeatability of the indentation modulus during sampling is a key factor that is frequently used to evaluate its reliability. If the target material exhibits pure elastic rebound upon complete unloading, it is very likely that the measured indentation modulus will approach the Young modulus. In this study, in fact, the indentation modulus E_{IT} measured at the core region of the SEBM-manufactured Ti-6Al-4V alloy disk was found to be very close to the Young modulus measured in the tensile test (see Figure 15). In the same figure, the Young modulus is shown in blue, whereas the indentation modulus is shown in red, green, and gray for the a-sample through to the d-sample, respectively. For convenience, the graph also includes the mean value (over three indentations) of the indentation modulus as a baseline (cyan line). The mean indentation modulus is 102 and 101 GPa for the c-sample and d-sample (the smallest value), respectively, and 128 and 114.5 GPa for the a-sample (the largest value) and b-sample, respectively. The individual values of the indentation modulus for all the samples were 127, 114, 102, and 100 GPa, that is, values which differ from the Young modulus by about 18%, 5%, 7%, and 13%, respectively, for the a-sample through to the d-sample. Thus, the Young modulus was able to approximate the indentation modulus to within an error of less than 20%.

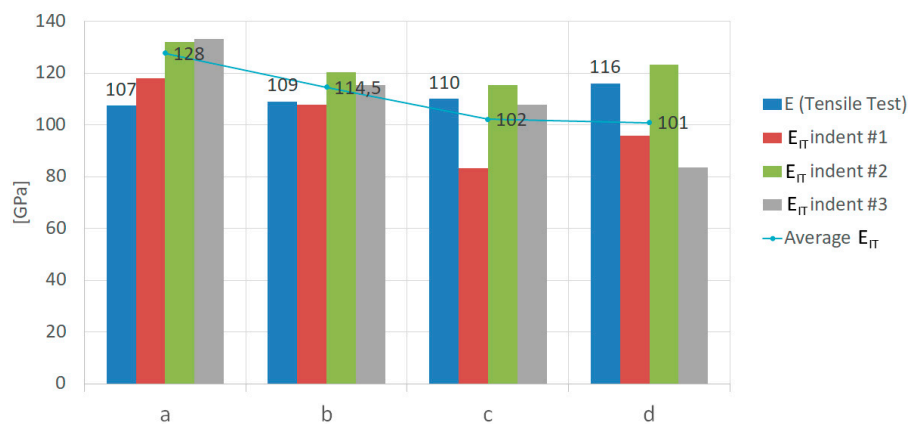


Figure 15. Comparison between Young modulus (E) and mean indentation modulus (E_{IT}) for three indents (300 N); average E_{IT} (baseline) has been computed as an average over the three indents.

By assuming the validity of the Tabor law [41], which relates the indentation hardness to a representative strength (RS), i.e., $RS = H_{IT}/3$ [17,42,43], and that RS tends to UTS for a Vickers indenter, it was possible to estimate a local (tensile-like) UTS at the core of each sample. The results are shown in Figure 16, along with the baseline curve given by the average value of RS over three indentations.

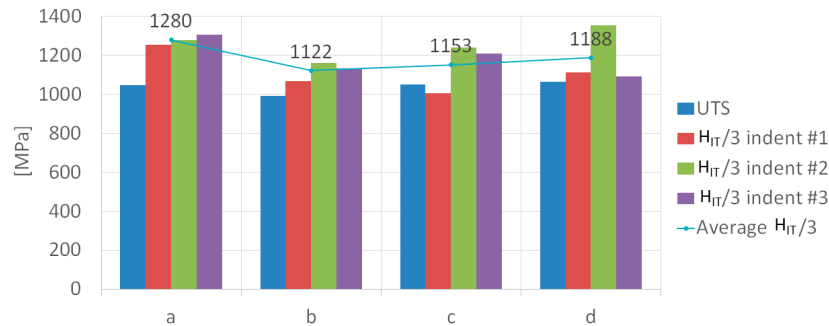


Figure 16. Comparison between UTS and representative stress from Tabor law ($H_{IT}/3$) for three indents (300 N); average H_{IT} (baseline) has been computed as an average over the three indents.

It has been shown that in all the samples, RS overestimated the actual UTS by an error of less than 20%, i.e., within a relatively small margin of error, meaning that a representative tensile-like UTS can be determined in SEBM-manufactured Ti-6Al-4V alloy builds at the local scale in a quick, easy, and non-destructive manner using the Tabor law.

Finally, Figure 17 depicts in one single graph the desired performance indices of the fabricated SEBM Ti-6Al-4V alloy at the local scale, including porosity, indentation hardness, and α -plate width, versus the two investigated process mode conditions, MM and BTM. The results in the previous sections underline that in general, the microstructure morphology did not change sensibly when switching from BTM to MM within the investigated limits. Furthermore, the MM samples (the b-, c-, and d-samples) exhibited clearly distinct indices for different beam currents and scan speeds.

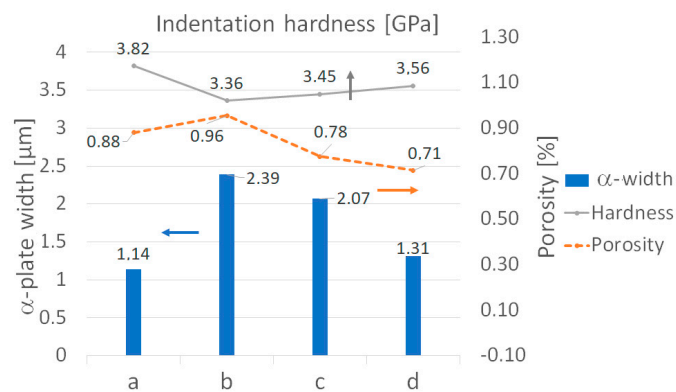


Figure 17. Correlation between indentation hardness at the sample center, α -plate width, and porosity for a–d samples.

The BTM mode ensured, at the local scale, fine microstructures ($\lambda = 1.14 \mu\text{m}$) and small residual porosity (0.88%), both of which are beneficial for an optimal combination of high strength (largest) and toughness. However, the MM mode provided quite different results, which can be rationalized and, possibly optimized, to expand the versatility of the SEBM process. Specifically, the b-sample presented a relatively coarse microstructure ($\lambda = 2.39 \mu\text{m}$), large residual porosity (0.96%), and lower hardness (the lowest value) as a result of intensive beam heating and limited cooling. The c-sample and the d-sample contained less residual porosity than the a-sample, but at the price of a coarser microstructure and lower local strength. On the other hand, the tensile tests gave clear evidence of the synergistic effect of macro-scale porosities (i.e., over the entire volume of the sample) and of the

microstructure on the mechanical properties, thereby reversing the scenario of bulk strength in favor of MM (c- and d-samples) over BTM (a-sample): most of the tensile properties (UTS, YS, E) of the MM samples (c-sample and d-sample) were larger than those of the BTM sample due to less residual porosity. As per the tensile ductility, which in metals generally requires a coarse microstructure and a low level of porosity to be maximized, with the latter being about 12% in all the samples, it turns out that the tensile ductility could not clearly be discriminated in either BTM or MM, except for the b-sample, which was affected by excessive porosity. Overall, the d-sample (MM) appeared to exhibit the optimal combination of porosity and microstructure on the mechanical properties, at both a micro and macro scale, being affected by the lowest beam current and scan speed investigated here.

4. Conclusions

The SEBM of a Ti-6Al-4V alloy has been investigated in this work under two processing modes, namely the built-in BTM (a-sample) and the user set MM (b-, c-, and d-samples) under specified limits of the beam current and scan speed variation range. The performances of both modes were compared, in terms of residual porosity, microstructure, and mechanical properties, at both a microscopic scale (core region) and a macroscopic (build) scale. Upon varying the beam current and scan speed, both the porosity and resolution of microstructure were affected to a great extent as a result of the different heating and cooling rates along the build direction.

By dividing the build thickness into three regions, namely, the bottom, center, and top, it was found that the residual porosity was minimal in the a-, c-, and d-samples, but was relatively large in the b-sample, whose soundness was impaired by the severe intensive heating and the subsequent low cooling rate condition. The BTM sample contained several unfused-layer defects and micro-porosities.

In general, at a sufficient distance from the build plate, a gradient microstructure, oriented along the build direction, was observed for both build modes. Both modes also shared the same basic solidification mechanism which was of the β -phase type. The gradient microstructure was finer in the BTM and the pores more populated as compared to the MM counterparts, except for the b-sample, which showed the largest porosity. The microstructure mainly consisted of columnar prior β -grains (delineated by α -phase boundaries) which embedded a nearly equilibrium $\alpha + \beta$ lamellar structure of a dominant α -phase (platelet type arranged either as a colony or as a basket weave pattern) embedded in a β -phase matrix. Such a lamellar structure resulted from the transformation annealing of the original β -phase upon final (second stage) cooling of the chamber from 730 °C to room temperature. No martensitic (α') structure was observed under any conditions.

As per the microstructure along the build direction, it was found that: the bottom part presented equiaxed prior β -grains (delineated by an α -phase boundary) embedding an equilibrium structure made of β -rods and α -lamellae (in the form of a colony or basket weave pattern), with this structure resulting from near uniform heating and an isotropic dissipation of the heat from the melting temperature to 730 °C of the build plate (the first cooling stage); the core region experienced a transition from an equiaxed to a columnar prior β -grain structure which embedded a finer $\alpha + \beta$ microstructure than that observed at the bottom as a result of higher cooling rates than at the bottom; the top part showed a marked columnar prior β -grain structure containing a highly resolved $\alpha + \beta$ lamellar structure which resulted from the strong-non equilibrium conditions and consequent hindered atomic diffusion induced by the faster heating and cooling.

The macro-scale tensile properties, measured on flat horizontally SEBM-manufactured Ti-6Al-4V alloy dog-bone samples, were in good agreement with literature values. Micro-scale indentation properties were measured at three separation distances from the build plate (bottom, center, and top) along the build direction by means of a macro-instrumented indentation test. The tensile-like indentation properties measured at the sample core (between the last deposited layer and the build plate) were consistent with the (macro) tensile properties.

Indentation hardness was larger in the a- and d-samples than in the b-sample and c-sample. It has been confirmed that indentation hardness increases as the α -plate width decreases. The indentation

modulus matched the Young modulus well. It was larger in the a- and d-samples than in the b- and c-samples. The representative stress, estimated by means of the Tabor law ($H_{IT}/3$), approached the UTS with an error <20% in all the samples. The correlation established between the residual porosity, microstructure, indentation properties, and process parameters confirms the best performances of the d-sample in terms of the net shape geometry (i.e., negligible distortion and bending/thermal stress), satisfactory microstructure resolution, and the optimal trade-off of the micro and macro scale mechanical properties.

As per the investigated process conditions, the BTM microstructure was quite fine compared to the MM samples, although the shape and size of the as-built (disk) sample was affected by pronounced thermal stresses and deformations. The d-sample exhibited the best combination of microstructure resolution, uniform distribution of small pores, and absence of unfused zones. Both the UTS and Young modulus of the BTM sample were lower than the optimal MM (d-) sample, whereas elongation to fracture was approximately equal for all the samples.

It may be finally stressed that MIIT provides a reliable and effective testing methodology to assess the mechanical properties of the build products as well as to accelerate the setup of the process, taking advantage of its easy, quick, and non-destructive testing features from the one hand and that of allowing, in the case of an SEBM-manufactured Ti-6Al-4V alloy, a link of local indentation properties to tensile properties from the other hand.

Author Contributions: All authors conceived and designed the experiments. C.P. and A.C. manufactured the specimens. G.M., C.P., and A.C. analyzed the results. G.M. and C.P. wrote the paper. C.P. and H.S. reviewed and edited the paper.

Funding: This work was supported by the German Research Foundation (DFG, grant number 1270/1, collaborative research center “ELAINE”).

Conflicts of Interest: The authors declare no conflict of interest.

References

1. Körner, C. Additive manufacturing of metallic components by selective electron beam melting—A review. *Int. Mater. Rev.* **2016**, *61*, 361–377. [[CrossRef](#)]
2. Guo, N.; Leu, M.C. Additive manufacturing: technology, applications and research needs. *Front. Mech. Eng. Chin.* **2013**, *8*, 215–243. [[CrossRef](#)]
3. Murr, L.E.; Quinones, S.A.; Gaytan, S.M.; Lopez, M.I.; Rodela, A.; Martinez, E.Y.; Hernandez, D.H.; Martinez, E.; Medina, F.; Wicker, R.B. Microstructure and mechanical behavior of Ti-6Al-4V produced by rapid-layer manufacturing, for biomedical applications. *J. Mech. Behav. Biomed. Mater.* **2009**, *2*, 20–32. [[CrossRef](#)] [[PubMed](#)]
4. Koike, M.; Martinez, K.; Guo, L.; Chahine, G.; Kovacevic, R.; Okabe, T. Evaluation of titanium alloy fabricated using electron beam melting system for dental applications. *J. Mater. Process. Technol.* **2009**, *211*, 1400–1408. [[CrossRef](#)]
5. Syam, W.P.; Al-Shehri, H.A.; Al-Ahmari, A.M.; Al-Wazzan, K.A.; Mannan, M.A. Preliminary fabrication of thin-wall structure of Ti-6Al-4V for dental restoration by electron beam melting. *Rapid Prototyping J.* **2012**, *18*, 230–240. [[CrossRef](#)]
6. Seifi, M.; Salem, A.; Beuth, J.; Harrysson, O.; Lewandowski, J.J. Overview of materials qualification needs for metal additive manufacturing. *JOM* **2016**, *68*, 747–764. [[CrossRef](#)]
7. Gorse, S.; Hutchinson, C.; Gouné, M.; Banerjee, R. Additive manufacturing of metals: a brief review of the characteristic microstructures and properties of steels, Ti-6Al-4V and high-entropy alloys. *Sci. Technol. Adv. Mater.* **2017**, *18*, 584–610. [[CrossRef](#)]
8. Murr, L.E.; Gaytan, S.M.; Ramirez, D.A.; Martinez, E.; Hernandez, J.; Amato, K.N.; Shindo, P.W.; Medina, F.R.; Wicker, R.B. Metal fabrication by additive manufacturing using laser and electron beam melting technologies. *J. Mater. Sci. Technol.* **2012**, *28*, 1–14. [[CrossRef](#)]
9. Neira-Arce, A. *Thermal Modeling and Simulation of Electron Beam Melting for Rapid Prototyping on Ti6Al4V Alloys*; North Carolina State University: Raleigh, NC, USA, 2012.

10. Puebla, K.; Murr, L.E.; Gaytan, S.M.; Martinez, E.; Medina, F.; Wicker, R.B. Effect of melt scan rate on microstructure and macrostructure for electron beam melting of Ti-6Al-4V. *Mater. Sci. Appl.* **2012**, *3*, 259. [[CrossRef](#)]
11. Tan, X.; Kok, Y.; Toh, W.Q.; Tan, Y.J.; Descoins, M.; Mangelinck, D.; Tor, S.B.; Leong, K.F.; Chua, C.K. Revealing martensitic transformation and α/β interface evolution in electron beam melting three-dimensional-printed Ti-6Al-4V. *Sci. Rep.* **2016**, *6*, 26039. [[CrossRef](#)]
12. Koike, M.; Greer, P.; Owen, K.; Lilly, G.; Murr, L.E.; Gaytan, S.M.; Martinez, E.; Okabe, T. Evaluation of titanium alloys fabricated using rapid prototyping technologies—Electron beam melting and laser beam melting. *Materials* **2011**, *4*, 1776–1792. [[CrossRef](#)] [[PubMed](#)]
13. Rafi, H.K.; Karthik, N.V.; Gong, H.; Starr, T.L.; Stucker, B.E. Microstructures and mechanical properties of Ti6Al4V parts fabricated by selective laser melting and electron beam melting. *J. Mater. Eng. Perform.* **2013**, *22*, 3872–3883. [[CrossRef](#)]
14. Weißmann, V.; Drescher, P.; Bader, R.; Seitz, H.; Hansmann, H.; Laufer, N. Comparison of single Ti6Al4V struts made using selective laser melting and electron beam melting subject to part orientation. *Metals* **2017**, *7*, 91. [[CrossRef](#)]
15. Hrabe, N.; Quinn, T. Effects of processing on microstructure and mechanical properties of a titanium alloy (Ti-6Al-4V) fabricated using electron beam melting (EBM), part 1: Distance from build plate and part size. *Mater. Sci. Eng., A* **2013**, *573*, 264–270. [[CrossRef](#)]
16. Gaytan, S.M.; Murr, L.E.; Medina, F.; Martinez, E.; Lopez, M.I.; Wicker, R.B. Advanced metal powder based manufacturing of complex components by electron beam melting. *Mater. Technol.* **2009**, *24*, 180–190. [[CrossRef](#)]
17. Zhang, P.; Li, S.X.; Zhang, Z.F. General relationship between strength and hardness. *Mater. Sci. Eng. A* **2011**, *529*, 62–73. [[CrossRef](#)]
18. Al-Bermani, S.S.; Blackmore, M.L.; Zhang, W.; Todd, I. The origin of microstructural diversity, texture, and mechanical properties in electron beam melted Ti-6Al-4V. *Metall. Mater. Trans. A* **2010**, *41*, 3422–3434. [[CrossRef](#)]
19. Mandil, G.; Paris, H.; Suard, M. Building new entities from existing titanium part by electron beam melting: microstructures and mechanical properties. *Int. J. Adv. Manuf. Technol.* **2016**, *85*, 1835–1846. [[CrossRef](#)]
20. Guo, C.; Ge, W.; Lin, F. Effects of scanning parameters on material deposition during Electron Beam Selective Melting of Ti-6Al-4V powder. *J. Mater. Process. Technol.* **2015**, *217*, 148–157. [[CrossRef](#)]
21. Safdar, A.; Wei, L.Y.; Snis, A.; Lai, Z. Evaluation of microstructural development in electron beam melted Ti-6Al-4V. *Mater. Charact.* **2012**, *65*, 8–15. [[CrossRef](#)]
22. Milberg, J.; Sigl, M. Electron beam sintering of metal powder. *Prod. Eng.* **2008**, *2*, 117–122. [[CrossRef](#)]
23. Weiwei, H.; Wenpeng, J.; Haiyan, L.; Huiping, T.; Xinting, K.; Yu, H. Research on preheating of titanium alloy powder in electron beam melting technology. *Rare Metal Mater. Eng.* **2011**, *40*, 2072–2075. [[CrossRef](#)]
24. Drescher, P.; Sarhan, M.; Seitz, H. An investigation of sintering parameters on titanium powder for electron beam melting processing optimization. *Materials* **2016**, *9*, 974. [[CrossRef](#)] [[PubMed](#)]
25. Tan, X.; Kok, Y.; Tan, Y.J.; Descoins, M.; Mangelinck, D.; Tor, S.B.; Leong, K.F.; Chua, C.K. Graded microstructure and mechanical properties of additive manufactured Ti-6Al-4V via electron beam melting. *Acta Mater.* **2015**, *97*, 1–16. [[CrossRef](#)]
26. Karlsson, J.; Snis, A.; Engqvist, H.; Lausmaa, J. Characterization and comparison of materials produced by Electron Beam Melting (EBM) of two different Ti-6Al-4V powder fractions. *J. Mater. Process. Technol.* **2013**, *213*, 2109–2118. [[CrossRef](#)]
27. Williams, T.; Zhao, H.; Léonard, F.; Derguti, F.; Todd, I.; Prangnell, P.B. XCT analysis of the influence of melt strategies on defect population in Ti-6Al-4V components manufactured by Selective Electron Beam Melting. *Mater. Charact.* **2015**, *102*, 47–61. [[CrossRef](#)]
28. Zhang, L.C.; Liu, Y.; Hao, Y. Additive manufacturing of Titanium alloys by Electron Beam Melting: A Review. *Adv. Eng. Mater.* **2018**, *20*, 1700842. [[CrossRef](#)]
29. Dinwiddie, R.B.; Kirka, M.M.; Lloyd, P.D.; Dehoff, R.R.; Lowe, L.E.; Marlow, G.S. Calibrating IR Cameras for in-Situ Temperature Measurement during the Electron Beam Melt Processing of Inconel 718 and Ti-Al6-V4. Proceeding of the Thermosense: Thermal Infrared Applications XXXVIII, Baltimore, MD, USA, 18–21 April 2016.
30. Raplee, J.; Plotkowski, A.; Kirka, M.M.; Dinwiddie, R.; Okello, A.; Dehoff, R.R.; Babu, S.S. Thermographic microstructure monitoring in electron beam additive manufacturing. *Sci. Rep.* **2017**, *7*, 43554. [[CrossRef](#)]

31. SridharBabu, B.; Kumaraswamy, A.; AnjaneyaPrasad, B. Effect of Indentation Size and Strain Rate on Nanomechanical Behavior of Ti-6Al-4VAlloy. *Trans. Indian Inst. Met.* **2015**, *68*, 143–150. [[CrossRef](#)]
32. Lancaster, R.; Davies, G.; Illsley, H.; Jeffs, S.; Baxter, G. Structural Integrity of an Electron Beam Melted Titanium Alloy. *Materials* **2016**, *9*, 470. [[CrossRef](#)]
33. International Organization for Standardization. *Metallic Materials: Instrumented Indentation Test for Hardness and Materials Parameters. Verification and Calibration of Testing Machines*; ISO: Geneva, Switzerland, 2002.
34. Chahine, G.; Koike, M.; Okabe, T.; Smith, P.; Kovacevic, R. The design and production of Ti-6Al-4V ELI customized dental implants. *JOM* **2008**, *60*, 50–55. [[CrossRef](#)]
35. Drescher, P.; Reimann, T.; Seitz, H. Investigation of powder removal of net-structured titanium parts made from electron beam melting. *Int. J. Rapid Manuf.* **2014**, *4*, 81–89. [[CrossRef](#)]
36. Delo, D.P.; Piehler, H.R. Early stage consolidation mechanisms during hot isostatic pressing of Ti-6Al-4V powder compacts. *Acta Mater.* **1999**, *47*, 2841–2852. [[CrossRef](#)]
37. Facchini, L.; Magalini, E.; Robotti, P.; Molinari, A. Microstructure and mechanical properties of Ti-6Al-4V produced by electron beam melting of pre-alloyed powders. *Rapid Prototyping J.* **2009**, *15*, 171–178. [[CrossRef](#)]
38. Froes, F.H. *Titanium Physical Metallurgy, Processing and Applications*; ASM International: Geauga County, OH, USA, 2015.
39. Cagliero, R.; Barbato, G.; Maizza, G.; Genta, G. Measurement of elastic modulus by instrumented indentation in the macro-range: Uncertainty evaluation. *Int. J. Mech. Sci.* **2015**, *101*, 161–169. [[CrossRef](#)]
40. Cagliero, R.; Maizza, G.; Barbato, G. Unconventional Mechanical Testing for process set up and product qualification in additive manufacturing. *Polaris Innov. J.* **2016**, *25*, 28–32.
41. Tabor, D. *The Hardness of Metals*; Clarendon Press: Oxford, UK, 1951.
42. Boyer, H.E.; Gall, T.L. *Metals Handbook: Desk Edition*; ASM International: Geauga County, OH, USA, 1985.
43. Callister, W.D.; Rethwisch, D.G. *Materials Science and Engineering: An Introduction*; John Wiley & Sons: New York, NY, USA, 2007; pp. 665–715.



© 2019 by the authors. Licensee MDPI, Basel, Switzerland. This article is an open access article distributed under the terms and conditions of the Creative Commons Attribution (CC BY) license (<http://creativecommons.org/licenses/by/4.0/>).